Superconducting Properties of Layered Cuprate Oxides

Masashi TACHIKI, Tomio KOYAMA and Saburo TAKAHASHI

Institute for Materials Research, Tohoku University, Sendai 980

(Received October 7, 1991)

Superconducting properties of cuprate superconductors are theoretically studied using a model in which superconductivity is primarily generated in the CuO_2 layers and superconductivity in the other layers is induced by the proximity effect. The anomalous temperature dependence of the Knight shifts and the nuclear magnetic relaxation rates for Cu and O ions in $YBa_2Cu_3O_7$ are explained by a theoretical result based on this model. The structure of the flux lines is very different depending on whether the flux lines are parallel or perpendicular to the layers. An unusual magnetization process in the mixed state follows the anomalous nature of the interaction between the flux lines.

§ 1. Introduction

Cuprate oxides which show high T_c-superconductivity have layer structures in which several kinds of oxide layers are periodically stacked along the c axis. As a result, their physical properties are highly anisotropic. For example, the electric conductivity along the layers is much larger than that along the c axis. Therefore, the crystals are considered to be constructed by conductive layers coupled by the relatively weak transfer interaction. For the superconducting state we take a model in which superconductivity is generated in the CuO_2 layers in the crystals, and superconductivity in the primarily non-superconducting layers is induced by the proximity effect.[1),2)] Using this model, we calculate the Knight shifts and the nuclear magnetic relaxation rates for the Cu and O ions in the CuO_2-plane layer and the CuO-chain layer of $YBa_2Cu_3O_7$.[3)] Both the quantities in the CuO_2-plane layer decrease much faster than those in the CuO-chain layer below the superconducting transition temperature. The agreement of the temperature dependence with that observed in the experiments confirms applicability of this layered model for the cuprate superconductors. For discussing the structure of the flux lines, we use a simplified model in which the superconductivity in the layers is described by the Ginzburg-Landau equation and the coupling between the layers by the Josephson coupling mechanism. This is a generalized Lawrence-Doniach model. The result of the calculation shows that the structure of the flux lines is very different depending on whether the flux lines are parallel or perpendicular to the layers.[4)] The H_{c1} versus temperature curve shows a pronounced upturn when temperature decreases.[5)] The anomalous interaction between the flux lines parallel to the layers is reflected by an unusual magnetization process in the mixed state.[6)]

§ 2. Model for the layered cuprate oxides

Since experimental studies have most extensively been done on $YBa_2Cu_3O_7$, we take the crystal as an example of the layered cuprate oxides. The crystal of $YBa_2Cu_3O_7$ is constructed by a stacking of two CuO_2-plane layers and one CuO-chain layer as shown in Fig. 1. The Y and Ba ions are neglected, since the electronic levels of these ions disappear near the Fermi level. The axes x, y and z are taken parallel to the crystal axes a, b and c, respectively. The chains are parallel to the axis y. We assume that the electronic bands of the CuO_2-plane and CuO-chain layers have two and one-dimensional dispersions, respectively, and electrons transfer between the layers by the electron transfer interaction. Then, the Hamiltonian of this system is written as

$$H=\sum_{\boldsymbol{k},\sigma}\{\varepsilon_a(\boldsymbol{k})[a^\dagger_{\boldsymbol{k}\sigma}a_{\boldsymbol{k}\sigma}+a'^\dagger_{\boldsymbol{k}\sigma}a'_{\boldsymbol{k}\sigma}]+\varepsilon_b(\boldsymbol{k})b^\dagger_{\boldsymbol{k}\sigma}b_{\boldsymbol{k}\sigma}\}$$
$$+\sum_{\boldsymbol{k},\sigma}\{t(\boldsymbol{k})[a^\dagger_{\boldsymbol{k}\sigma}b_{\boldsymbol{k}\sigma}+b^\dagger_{\boldsymbol{k}\sigma}a'_{\boldsymbol{k}\sigma}]+t'(\boldsymbol{k})a'^\dagger_{\boldsymbol{k}\sigma}a_{\boldsymbol{k}\sigma}+\text{h.c.}\}$$
$$+\varDelta\sum_{\boldsymbol{k}}(a_{\boldsymbol{k}\uparrow}a_{-\boldsymbol{k}\downarrow}+a'_{\boldsymbol{k}\uparrow}a'_{-\boldsymbol{k}\downarrow}+\text{h.c.})\,, \tag{1}$$

where $a_{\boldsymbol{k}\sigma}$ and $a'_{\boldsymbol{k}\sigma}$ are the annihilation operators of particles in the planes and $b_{\boldsymbol{k}\sigma}$ is that in the chain layer, respectively, and $\varepsilon_a(\boldsymbol{k})$ and $\varepsilon_b(\boldsymbol{k})$ are the energy dispersions of these particles. The transfer interaction parameters $t(\boldsymbol{k})$ and $t'(\boldsymbol{k})$ in Eq. (1) are defined by

$$t(\boldsymbol{k})=-t_1\exp(ik_zc_1)\,,\quad t'(\boldsymbol{k})=-t_2\exp(ik_zc_2)\,, \tag{2}$$

where t_1 is the transfer integral between the plane and chain layers and t_2 is the transfer integral between the planes, and c_1 and c_2 are the distance between the plane and chain layers and the distance between the plane layers, respectively. The layer nature of the oxides arises when the transfer integrals between these layers are small. Since the carriers are holes in $YBa_2Cu_3O_7$, we assume the forms

$$\varepsilon_a(\boldsymbol{k})=-\frac{\hbar^2}{2m_a}(k_x{}^2+k_y{}^2-k_a{}^2)\,,$$
$$\varepsilon_b(\boldsymbol{k})=-\frac{\hbar^2}{2m_b}(k_y{}^2-k_b{}^2)\,, \tag{3}$$

where m_a and m_b are, respectively, the effective masses of the particles in the plane and chain layers, and k_a and k_b are parameters. In Eq. (3), the values of k_x and k_y are restricted to the region, $|k_x|\le k_c$, $|k_y|\le k_c$ with a cutoff momentum k_c.

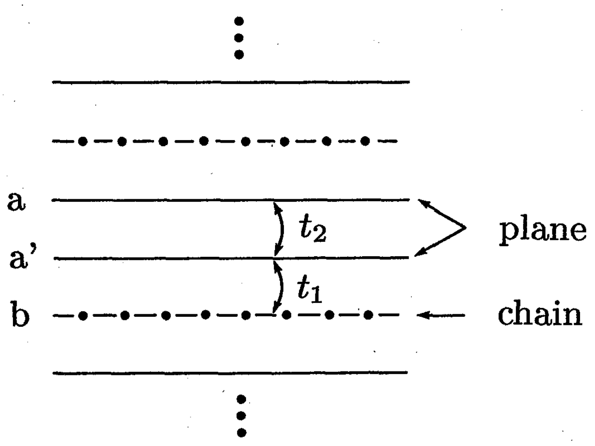

Fig. 1. Model crystal structure of $YBa_2Cu_3O_7$. The solid and dot-dashed lines denote the CuO_2-plane and CuO-chain layers, respectively.

In Eq. (1), we assume an isotropic pairing interaction with a superconducting gap parameter Δ in the CuO_2 layers and no pairing interaction in the chain layers. In the following, we use the parameter values; $m_a/m_b=1$, $k_a/k_c=0.8$, $k_b/k_c=0.7$ and $t_1/\varepsilon_c=t_2/\varepsilon_c=0.1$, where ε_c is the cutoff energy defined by $\varepsilon_c=\hbar^2k_c^2/2m_a$.

Introducing a Nambu representation

$$A_{\boldsymbol{k}}=\begin{pmatrix} A_{\boldsymbol{k}1} \\ A_{\boldsymbol{k}2} \\ A_{\boldsymbol{k}3} \\ A_{\boldsymbol{k}4} \\ A_{\boldsymbol{k}5} \\ A_{\boldsymbol{k}6} \end{pmatrix}=\begin{pmatrix} a_{\boldsymbol{k}\uparrow} \\ a^{\dagger}_{-\boldsymbol{k}\downarrow} \\ b_{\boldsymbol{k}\uparrow} \\ b^{\dagger}_{-\boldsymbol{k}\downarrow} \\ a'_{\boldsymbol{k}\uparrow} \\ a'^{\dagger}_{-\boldsymbol{k}\downarrow} \end{pmatrix}, \tag{4}$$

we write the Hamiltonian H as

$$H=\sum_{\boldsymbol{k}}A_{\boldsymbol{k}}{}^{\dagger}QA_{\boldsymbol{k}}+\sum_{\boldsymbol{k}}(2\varepsilon_a(\boldsymbol{k})+\varepsilon_b(\boldsymbol{k})) \tag{5}$$

with

$$Q=\begin{pmatrix} \varepsilon_a(\boldsymbol{k}) & \Delta & t(\boldsymbol{k}) & 0 & t'^*(\boldsymbol{k}) & 0 \\ \Delta & -\varepsilon_a(\boldsymbol{k}) & 0 & -t(\boldsymbol{k}) & 0 & -t'^*(\boldsymbol{k}) \\ t^*(\boldsymbol{k}) & 0 & \varepsilon_b(\boldsymbol{k}) & 0 & t(\boldsymbol{k}) & 0 \\ 0 & -t^*(\boldsymbol{k}) & 0 & -\varepsilon_b(\boldsymbol{k}) & 0 & -t(\boldsymbol{k}) \\ t'(\boldsymbol{k}) & 0 & t^*(\boldsymbol{k}) & 0 & \varepsilon_a(\boldsymbol{k}) & \Delta \\ 0 & -t'(\boldsymbol{k}) & 0 & -t^*(\boldsymbol{k}) & \Delta & -\varepsilon_a(\boldsymbol{k}) \end{pmatrix}. \tag{6}$$

Diagonalizing the Hermite matrix Q by a unitary transformation

$$(U^{\dagger}QU)_{ij}=E_j(\boldsymbol{k})\delta_{ij}\,, \tag{7}$$

we have

$$H=\sum_{\boldsymbol{k}}\sum_{\mu=1}^{6}E_{\mu}(\boldsymbol{k})\gamma^{\dagger}_{\boldsymbol{k}\mu}\gamma_{\boldsymbol{k}\mu}+\sum_{\boldsymbol{k}}(2\varepsilon_a(\boldsymbol{k})+\varepsilon_b(\boldsymbol{k}))\,, \tag{8}$$

where $\gamma_{\boldsymbol{k}\mu}$ is the quasiparticle operator in the superconducting state

$$\gamma_{\boldsymbol{k}\mu}=\sum_{j=1}^{6}(U^{\dagger})_{\mu j}A_{\boldsymbol{k}j}\,. \tag{9}$$

The vector $(U_{1\mu}, U_{2\mu}, \cdots, U_{6\mu})$ is the eigenvector for the eigenvalue $E_{\mu}(\boldsymbol{k})$. The eigenvalues form three bands in each of the positive and negative energy regions and their energy dispersions are symmetric with respect to the Fermi level. Two of them have nearly two-dimensional dispersions and the other has a nearly one-dimensional dispersion. Each band has the superconducting energy gap around the Fermi level.

§ 3. Non-local susceptibility

For calculating the Knight shift and the nuclear relaxation rate, we need the non-local susceptibility.

$$\chi_{mm'}(\boldsymbol{q}, \omega)=-\mu_B{}^2\int_0^\infty dt\langle[\sigma_m{}^z(\boldsymbol{q}, t), \sigma_{m'}^z(-\boldsymbol{q}, 0)]\rangle\exp(i\omega t)\,, \tag{10}$$

where $\langle\cdots\rangle$ denotes the thermal average, μ_B the Bohr magneton, $[A, B]$ the commutator $AB-BA$, and $\sigma_m{}^z(\boldsymbol{q})$ the Fourier component of the spin density operator at the m layer. The susceptibility (10) is calculated as

$$\chi_{mm'}(\boldsymbol{q}, \omega)=\frac{\mu_B{}^2}{N}\sum_{\boldsymbol{k}}\sum_{i_m, j_{m'}}\int_{-\infty}^\infty d\omega_1\int_{-\infty}^\infty d\omega_2 \times\rho_{i_m j_{m'}}(\boldsymbol{k}+\boldsymbol{q}, \omega_1)\rho_{j_{m'} i_m}(\boldsymbol{k}, \omega_2)\frac{f(\omega_1)-f(\omega_2)}{\omega+\omega_2-\omega_1+i\delta}\,, \tag{11}$$

where $f(\omega)$ is the Fermi distribution function and $\rho_{ij}(\boldsymbol{k}, \omega)$ is expressed as

$$\rho_{ij}(\boldsymbol{k}, \omega)=\sum_{\mu=1}^{6} U_{i\mu}^*(\boldsymbol{k})U_{j\mu}(\boldsymbol{k})\delta(\omega-E_\mu(\boldsymbol{k}))\,. \tag{12}$$

In Eq. (11), i_m takes 1 and 2 for $m=a$, 3 and 4 for $m=b$, and 5 and 6 for $m=a'$, and similarly $j_{m'}$ takes 1 and 2 for $m'=a$, 3 and 4 for $m'=b$, and 5 and 6 for $m'=a'$. The susceptibility (11) is used to calculate the Knight shift in § 4 and the relaxation rate in § 5.

§ 4. Knight shift

The temperature dependence of the spin Knight shift $K_s(T)$ gives information about the magnitude of the superconducting energy gap and the symmetry of the pairing. The uniform spin susceptibility of the m layer is given by

$$\chi_m(T)=\sum_{m'}\chi_{mm'}(0, 0)\,. \tag{13}$$

The susceptibility (13) is calculated using Eq. (11) as

$$\chi_m(T)=\frac{\mu_B{}^2}{2T}\int_{-\infty}^\infty d\omega N_m(\omega)\mathrm{sech}^2\left(\frac{\omega}{2T}\right), \tag{14}$$

where $N_m(\omega)$ is the local density of states in the m layer

$$N_m(\omega)=\frac{1}{N}\sum_{\boldsymbol{k}}\rho_{i_m i_m}(\boldsymbol{k}, \omega)\,, \tag{15}$$

where i_m takes 1 for $m=a$, 3 for $m=b$, and 5 for $m=a'$, respectively. In Fig. 2 we show the calculated result of the local densities of states in the CuO_2-plane and CuO-chain layers. As seen in Fig. 2, the large energy gap opens at the plane layer and the small gap does at the chain layer. The latter arises from the proximity-induced superconductivity in the chain layer.

In calculating the temperature dependence of $\chi_m(T)$, we use the superconducting gap parameter whose temperature dependence is expressed by an interpolation formula[7)]

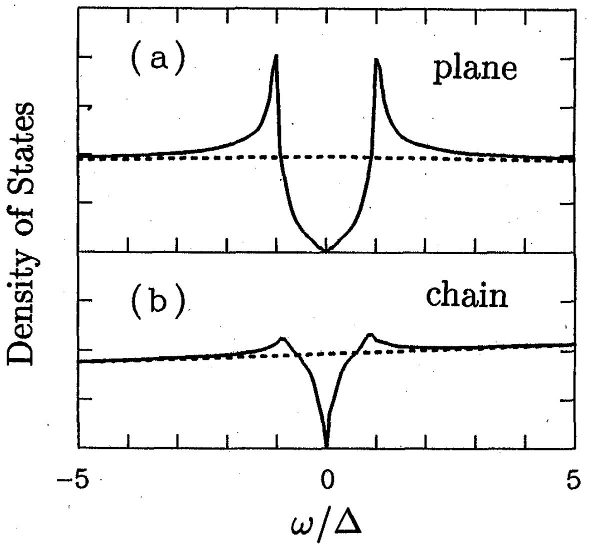

Fig. 2. Densities of states. (a) and (b) show the densities of states at the plane and chain layers, respectively. The solid and dashed curves indicate the densities of states in the superconducting and normal state, respectively.

$$\Delta(T)=\Delta(0)\tanh\left[\beta\left(\frac{T_c-T}{T}\right)^{1/2}\right] \tag{16}$$

with parameters $\Delta(0)$ and β. In this paper, we use the values of $2\Delta(0)/T_c=6.5$ (a strong coupling value), $\beta=1.74$ (the BCS value), and $T_c/\varepsilon_c=0.005$. Since the spin Knight shift is proportional to the spin susceptibility, $K_m^s(T)/K_m^s(T_c)=\chi_m(T)/\chi_m(T_c)$, where $K_m^s(T)$ is the spin Knight shift at the m layer. The calculated spin Knight shifts in the plane and chain layers are shown by the solid curves in a normalized form in Figs. 3(a) and (b), respectively. As seen in Fig. 3, the shift for the ions in the plane layers decreases more steeply than that of the BCS theory below T_c, whereas the shift in the chain layers decreases more gradually than that of the BCS theory. We obtain the experimental spin Knight shifts for the ^{63}Cu and ^{17}O ions in $YBa_2Cu_3O_7$, subtracting the orbital Knight shifts. The experimental values normalized at T_c are shown by the solid circles and triangles in Fig. 3. The agreement between the experiment and the theory is quite satisfactory.

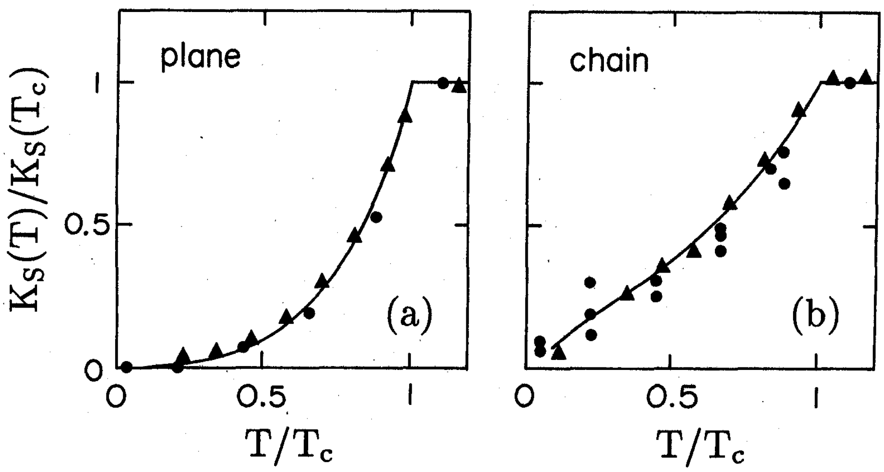

Fig. 3. Normalized Knight shifts of the Cu and O ions in the plane and chain layers. The symbols ● and ▲ are the experimental values of the normalized spin-Knight shifts for ^{63}Cu and ^{17}O in $YBa_2Cu_3O_7$, respectively. ● after Ref. 8), and ▲ after Ref. 9). The solid curves indicate the theoretical values.

§ 5. Nuclear relaxation rate

The low frequency spin fluctuations are responsible for the nuclear relaxation rate $1/T_1$. The nuclear relaxation rate at the m layer $1/T_{1m}$ is expressed as

$$\frac{1}{T_{1m}}=\frac{\gamma_N^2 T}{N}\sum_q |A_m(\boldsymbol{q})|^2 \mathrm{Im}\frac{X_{mm}(\boldsymbol{q},\omega_0)}{\omega_0}, \tag{17}$$

where γ_N is the nuclear gyromagnetic ratio, $A_m(\boldsymbol{q})$ is the hyperfine interaction constant between the nuclear spin and the $\boldsymbol{q}$ component of the spin fluctuation, and ω_0 is the nuclear magnetic resonance frequency. In Eq. (17), we assume that $A_m(\boldsymbol{q})$ is independent of q_z or there is no transfer hyperfine interaction between the layers. Our numerical calculation shows that the temperature dependence of $\mathrm{Im}\chi_{mm}(\boldsymbol{q},\omega_0)$ for the system described by the Hamiltonian (8) is almost independent of the wave number $\boldsymbol{q}$ below T_c. In this case, the nuclear relaxation rate (17) is approximately written as

$$\frac{1}{T_{1m}}=\left(\frac{1}{T_{1m}}\right)_{T_c}\cdot\frac{T}{T_c}\cdot\frac{\langle(\mathrm{Im}\chi_{mm}(\boldsymbol{q},\omega_0))_T\rangle_{\mathrm{av}}}{\langle(\mathrm{Im}\chi_{mm}(\boldsymbol{q},\omega_0))_{T_c}\rangle_{\mathrm{av}}} \tag{18}$$

with

$$\left(\frac{1}{T_{1m}}\right)_{T_c}=\frac{\gamma_N^2 T_c}{N}\sum_q |A_m(\boldsymbol{q})|^2 \mathrm{Im}\left(\frac{\chi_{mm}(\boldsymbol{q},\omega_0)}{\omega_0}\right)_{T_c}. \tag{19}$$

In Eq. (18), $\langle A\rangle_{\mathrm{av}}$ denotes the average value of A in the $\boldsymbol{q}$ space.

We numerically calculate $1/T_{1m}$ with use of a relation applicable to the case of a small value of ω_0

$$\sum_q \mathrm{Im}\frac{\chi_{mm}(\boldsymbol{q},\omega_0)}{\omega_0}\propto\sum_{im,jm}\int_{-\infty}^{\infty}d\omega\,\rho_{imjm}(\omega)\rho_{jmim}(\omega)\,\frac{1}{4T}\mathrm{sech}^2\left[\frac{\omega}{2T}\right] \tag{20}$$

with

$$\rho_{ij}(\omega)=\sum_k \rho_{ij}(\boldsymbol{k},\omega). \tag{21}$$

In the numerical calculation the δ-function in $\rho_{ij}(\omega)$ is replaced by a Lorentzian $(\gamma/\pi)/(\omega^2+\gamma^2)$ with $\gamma/\Delta(0)=0.08$. Figure 4 shows a log-log plot of the normalized relaxation rates in the plane and chain layers. The Hebel-Slichter peak appears just below T_c due to the gap opening in the plane layer. The magnitude of the peak is much smaller than that expected from the BCS theory. This fact is due to the following reasons. The Hebel-Slichter peak is constrained to the narrow temperature region just below T_c, since the superconducting order parameter $\Delta(T)$ steeply increases below T_c for a large value of $2\Delta(0)/T_c$ such as 6.5. The small peak may be eliminated by the lifetime effects due to spin and charge fluctuations, and phonons.[10)~12)] As seen from Fig. 4(a), the relaxation rate in the plane layers rapidly decreases below the peak. On the other hand, the temperature dependence of the relaxation rate in the chain layer is much weaker than that in the plane layer and no Hebel-Slichter peak is seen. This is because the superconductivity in the chain layer is much weaker and it has a gapless nature as seen in Fig. 2(b). The experimental values of the normalized relaxation rate for $YBa_2Cu_3O_7$ are shown in Fig. 4.

As seen in Figs. 3 and 4, a remarkable feature is that the experimental values of the normalized spin Knight shifts and relaxation rates for the Cu and O ions in each layer are on universal curves in the superconducting state. This fact indicates that

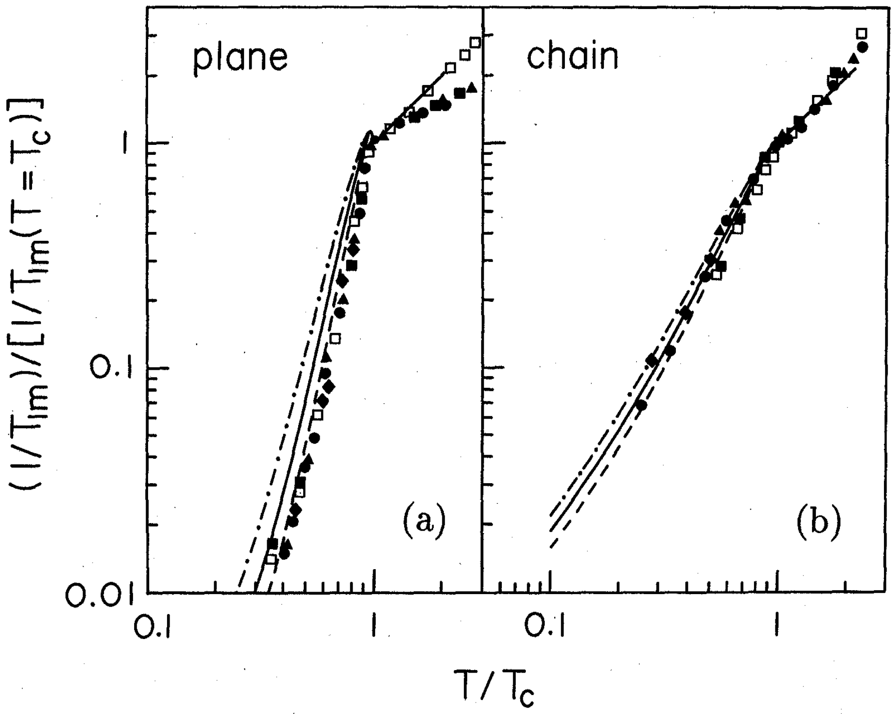

Fig. 4. Normalized nuclear relaxation rates of the Cu and O ions in the plane and chain layers. The solid and open symbols are the experimental values for ^{63}Cu and ^{17}O in $YBa_2Cu_3O_7$, respectively. ◆ after Ref. 13), ▲ after Ref. 14), ● after Ref. 15), and ■ and □ after Ref. 16). The dash-dotted, solid and dashed curves indicate the theoretical values for $2\Delta(0)/T_c=5.5$, 6.5 and 7.5, respectively.

the spin susceptibility responsible for the spin-Knight shift and the nuclear relaxation is common to the Cu and O ions in each layer.

§ 6. Mixed state in layered superconductors

To investigate unusual properties of the mixed state in high-T_c cuprate oxides we develop a phenomenological theory describing the flux lines in layered superconductors in this section. Consider a superconductor consisting of a periodic array of superconducting and normal (or weakly superconducting) layers, in which the layers are equally separated by a distance D. The current flowing across the layers is assumed to be of the Josephson type. The Ginzburg-Landau free energy of the superconductor is then expressed in terms of the order parameters defined on each layer, the Ψ_l's and the vector potential, $\boldsymbol{A}(\boldsymbol{r}, z)=(\boldsymbol{A}_{/\!/}(\boldsymbol{r}, z), A_z(\boldsymbol{r}, z))$,

$$
\begin{aligned}
F=\int d\boldsymbol{r}D\sum_l\Big[&\alpha_l(T)|\Psi_l(\boldsymbol{r})|^2+\frac{1}{2}\beta_l|\Psi_l(\boldsymbol{r})|^4\\
&+\frac{1}{4m_l}\left|\left(\frac{\partial}{\partial\boldsymbol{r}}-\frac{2ie}{c}\boldsymbol{A}_{/\!/}(\boldsymbol{r}, z_l)\right)\Psi_l(\boldsymbol{r})\right|^2\\
&+\frac{1}{4M_{l,l+1}D^2}\left|\Psi_{l+1}(\boldsymbol{r})\exp\left[-\frac{2ie}{c}\int_{z_l}^{z_{l+1}}dzA_z(\boldsymbol{r}, z)\right]-\Psi_l(\boldsymbol{r})\right|^2\Big]\\
&+\int d\boldsymbol{r}dz\frac{1}{8\pi}\boldsymbol{B}(\boldsymbol{r}, z)^2
\end{aligned}
\tag{22}
$$

with $z_l = lD$. Here, m_l is the effective mass on the lth layer, $M_{l,l+1}$ is the inverse interlayer coupling constant between the lth and $(l+1)$th layers with the units of mass, and $\alpha_l(T)$ and β_l are the GL coefficients on the lth layer. α_l is assumed to have the form

$$\alpha_l(T) = a_l(T - T_l^{(0)}), \tag{23}$$

$T_l^{(0)}$ being the transition temperature of the lth layer without an interlayer coupling. This is an extension of the Lawrence-Doniach model to the case of superconductors with nonequivalent layers. The in-plane coherence length and the in-plane penetration depth can be defined on each layer

$$\xi_l^2 = \frac{1}{4m_l|\alpha_l(T)|}, \tag{24}$$

$$\lambda_l^2 = \frac{m_l c^2 \beta_l}{8\pi e^2|\alpha_l(T)|}. \tag{25}$$

In the present model ξ_l and λ_l are sorted respectively into two independent parameters by whether the lth layer is superconducting or normal one, i.e., $\xi_l = \{\xi_S, \xi_N\}$ and $\lambda_l = \{\lambda_S, \lambda_N\}$.

(1) *$H /\!/ z$-axis case*

First we investigate a single flux line state when the magnetic field is applied in the direction perpendicular to the layers and calculate the lower critical field H_{c1}. The Ginzburg-Landau equations for the single flux line state are obtained from Eq. (22) in the cylindrical coordinates (r, θ, z) as

$$\frac{1}{4m_l}\left[\frac{1}{r}\frac{d}{dr}\left(r\frac{d}{dr}\phi_l(r)\right) - \frac{1}{r^2}Q_l^2(r)\phi_l(r)\right]$$
$$= -\eta_{l,l+1}\phi_{l+1} + [\alpha_l(T) + \eta_{l,l+1} + \eta_{l,l-1}]\phi_l(r) - \eta_{l,l-1}\phi_{l-1}(r) + \beta_l\phi_l^3(r), \tag{26}$$

$$r\frac{\partial}{\partial r}\left[\frac{1}{r}\frac{\partial}{\partial r}Q(r,z)\right] + \frac{\partial^2}{\partial z^2}Q(r,z) = D\sum_l\left(\frac{8\pi e^2}{m_l c^2}\right)\delta(z - z_l)Q_l(r)\phi_l^2(r), \tag{27}$$

where $\eta_{l,l+1} = 1/(4M_{l,l+1}D^2)$, $Q(r,z) = 1 - (2e/c)rA_\theta(r,z)$, $Q_l(r) = Q(r, z_l)$ and $\phi_l(r)$ is the amplitude of the order parameter, i.e., $\Psi_l(\boldsymbol{r}) = e^{i\theta}\phi_l(r)$. When the GL parameter $\kappa_S = \lambda_S/\xi_S$ is large, Eqs. (26) and (27) yield the following asymptotic solution to the order parameter for $\rho = r/\lambda_S \to \infty$,

$$\phi_l(r) = \left(\Delta_{M,l} - \frac{A_l}{\kappa_S \rho^2}\right)\left(\frac{|\alpha_S(T)|}{\beta_S}\right)^{1/2}, \tag{28}$$

where $\Delta_{M,l}$ is the order parameter in the Meissner state and A_l is a constant expressed in terms of the GL coefficients. Since the lower critical field is related to the free energy of the single flux line state, F_{Single}, by the relation, $H_{c1} = 4\pi F_{\mathrm{Single}}/\phi_0$ with $\phi_0 = hc/2e$, substitution of Eq. (28) into Eq. (22) leads to the following approximate expression for H_{c1} in the high-κ limit,

$$H_{c1} = \frac{1}{4\pi}\Gamma(T)\log\kappa_S\left[\frac{\phi_0}{\lambda_S(T)^2}\right], \tag{29}$$

where

$$\Gamma(T)=\frac{1}{L}\sum_{k=1}^{L}\left[\frac{\alpha_k(T)}{\alpha_S(T)}\Delta_{M,k}A_k-\frac{2m_S\lambda_S^2}{\kappa_S^2M_{k,k+1}D^2}(\Delta_{M,k+1}-\Delta_{M,k})(A_{k+1}-A_k)\right], \quad (30)$$

L being the period of the layer structure. It is understood that the factor $\Gamma(T)$ gives an additional temperature dependence arising from the layer structure to the temperature dependence of H_{c1}.

To understand the characteristic feature of the superconductivity in layered superconductors containing normal layers we first show the temperature dependence of $\Delta_{M,S}$ and $\Delta_{M,N}$, the order parameters of the superconducting and normal layers in the Meissner state. In Fig. 5, $\Delta_{M,S}$ and $\Delta_{M,N}$ are plotted in a case $L=3$, where the unit cell is composed of one superconducting and two normal layers. The transition temperature of the normal layers without an interlayer coupling was chosen to be zero in this case ($T_N^{(0)}=0$), that is, we consider the case where the superconductivity on the normal layers is induced by the coupling with the superconducting layers. As seen in this figure, the order parameter of the normal layers is much smaller than that of the superconducting layers at high temperatures near T_c. In this temperature range the superconducting order is maintained mostly by the superconducting layers. However, the superconducting order on the normal layers rapidly grows with decreasing temperature, so that both the superconducting and normal layers contribute to the superconducting condensation energy in the low temperature region.

In Fig. 6 we show the temperature dependence of H_{c1} calculated from Eq. (29) in the cases $L=2\sim5$. It is seen that an upturn curvature appears in the temperature dependence of H_{c1}. This upturn is understood as follows. Consider a flux line orthogonal to the layers. In this configuration the vortex core penetrates both the normal and superconducting layers. Since at high temperatures the superconducting order develops only in the superconducting layers, the increase in energy caused by creating a vortex core comes mainly from the superconducting layers. On the other hand, at low temperatures the superconducting order develops both in the normal and superconducting layers. As a result, forming a single flux line state at low temperatures costs more energy, so that H_{c1} rapidly increases as the temperature decreases. In single crystals of high-T_c oxides the similar temperature dependence has been observed.[17),18)]

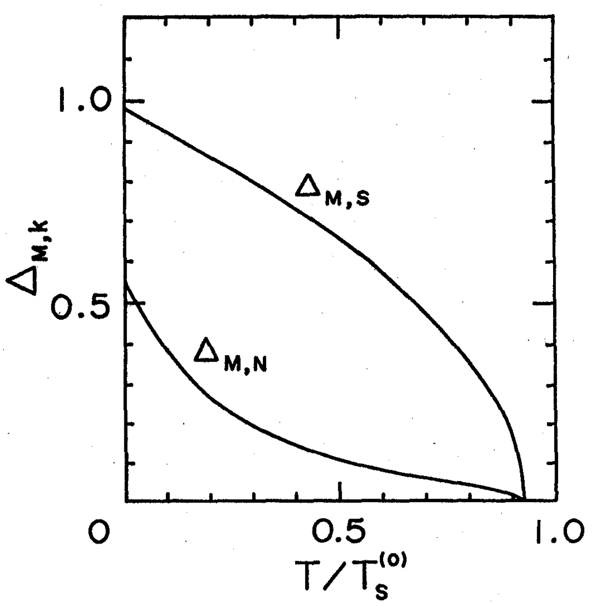

Fig. 5. Temperature dependence of the order parameters on the superconducting and normal layers in the Meissner state.

(2) *$H\perp z$-axis case*

Let us investigate the flux line states in the region near H_{c1} when the magnetic field is applied parallel to the layers

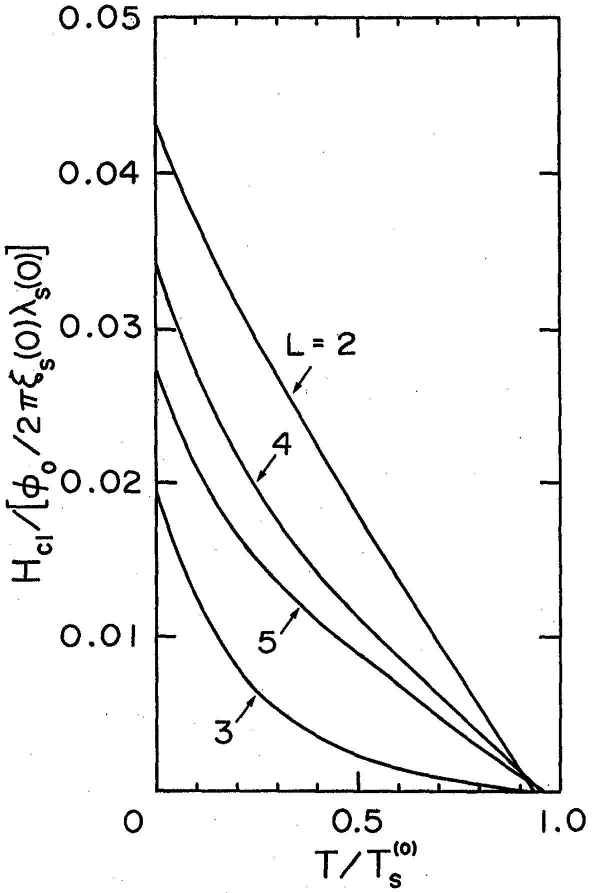

Fig. 6. Temperature dependence of H_{c1} in the direction perpendicular to the layers.

(along the x-axis). In the following we approximate the order parameter in the form

$$\Psi_l(y)\simeq\phi_l\exp[i\varphi_l(y)]\,, \tag{31}$$

neglecting the spatial dependence of the amplitude of $\Psi_l(y)$. This approximation is valid for the high-κ superconductors. The free energy (22) is, then, reduced to

$$F=\int dyD\sum_l\Big[\frac{1}{8\pi\lambda_l}Q_l(y)^2-\Big(\frac{\phi_0}{2\pi}\Big)^2 \times\frac{1}{4\pi\Gamma_{l,l+1}^2D^2}[1-\cos P_{l,l+1}(y)]\Big] +\int dydz\frac{1}{8\pi}B_x(y,z)^2\,, \tag{32}$$

where

$$Q_l(y)=\frac{\phi_0}{2\pi}\partial_y\varphi_l(y)-A_y(y,z_l)\,, \tag{33}$$

$$P_{l,l+1}(y)=\varphi_{l+1}(y)-\varphi_l(y)-\frac{2\pi}{\phi_0}\times\int_{z_l}^{z_{l+1}}dzA_z(y,z) \tag{34}$$

and

$$\Gamma_{l,l+1}^2=\frac{M_{l,l+1}c^2\sqrt{\beta_l\beta_{l+1}}}{8\pi e^2\sqrt{|\alpha_l\alpha_{l+1}|}}\,. \tag{35}$$

The variation of the free energy (32) with respect to the vector potential yields the equations,

$$B_l(y)-B_{l-1}(y)=\frac{DQ_l(y)^2}{\lambda_l^2}\,, \tag{36}$$

$$\partial_yB_l(y)=-\frac{\phi_0}{2\pi}\sin P_{l,l+1}(y)/(\Gamma_{l,l+1}^2D)\,. \tag{37}$$

Here $B_l(y)$ is the internal field in between the lth and $(l+1)$th layers,

$$B_x(y,z)=\sum_l[\theta(z-z_l)-\theta(z-z_{l+1})]B_l(y)\,. \tag{38}$$

Consider the single flux line state first. Eliminating the vector potential in $Q_l(y)$ and $P_{l,l+1}(y)$, we obtain the equation for $B_l(y)$ from Eqs. (36) and (37) for the single flux line state,

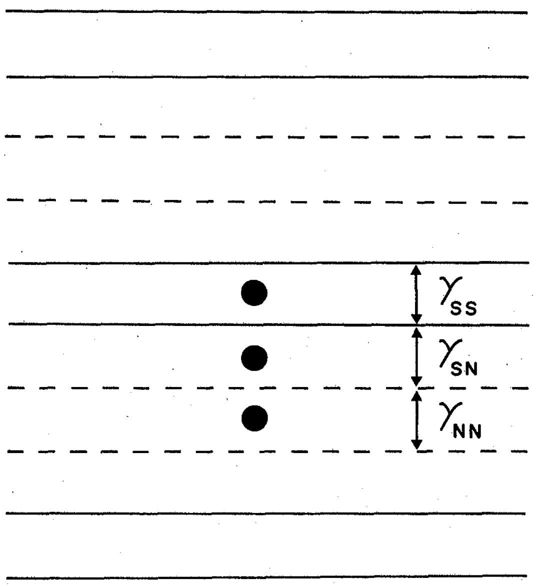

Fig. 7. The layer structure with a periodic array of superconducting layers (solid lines) and normal ones (broken lines). The black circles indicate three inequivalent positions of the flux line parallel to the layers.

$$\partial_y \sin^{-1}\left[\frac{2e}{c} D\Gamma_{l,l+1}^2 \partial_y B_l(y)\right] + \frac{2\pi}{cD} \times [\lambda_{l+1}^2 B_{l+1}(y) - (\lambda_{l+1}^2 + \lambda_l^2 + D^2) \times B_l(y) + \lambda_{l-1}^2 B_{l-1}(y)] = -2\pi\delta_{l,0}\delta(y)\,. \tag{39}$$

Here we assumed that the single flux line is located at $y=0$ between the zeroth ($l=0$) and its neighboring first ($l=1$) layer. We numerically solved Eq. (39) for the superconductor with a periodic array of pairs of two superconducting and two normal layers as shown in Fig. 7. In this case the flux line can take three inequivalent positions (S-S, S-N and N-N) if we assume that the single flux line is placed in between adjacent layers.

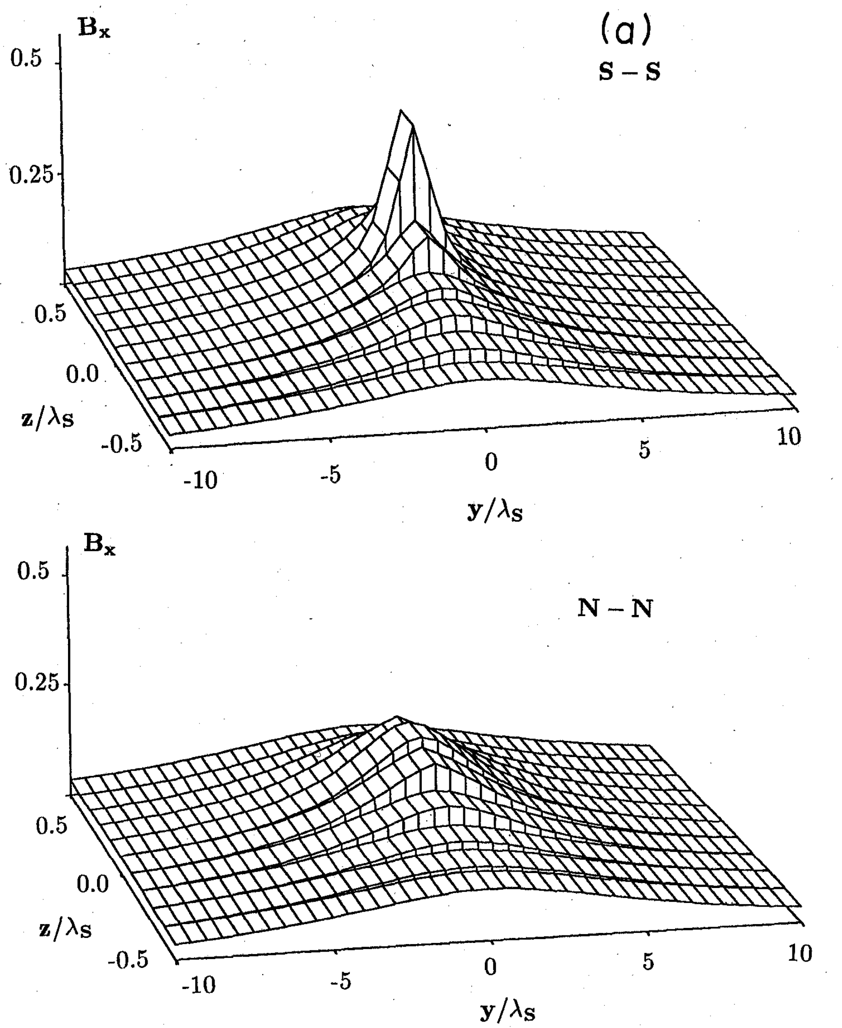

Fig. 8. (continued)

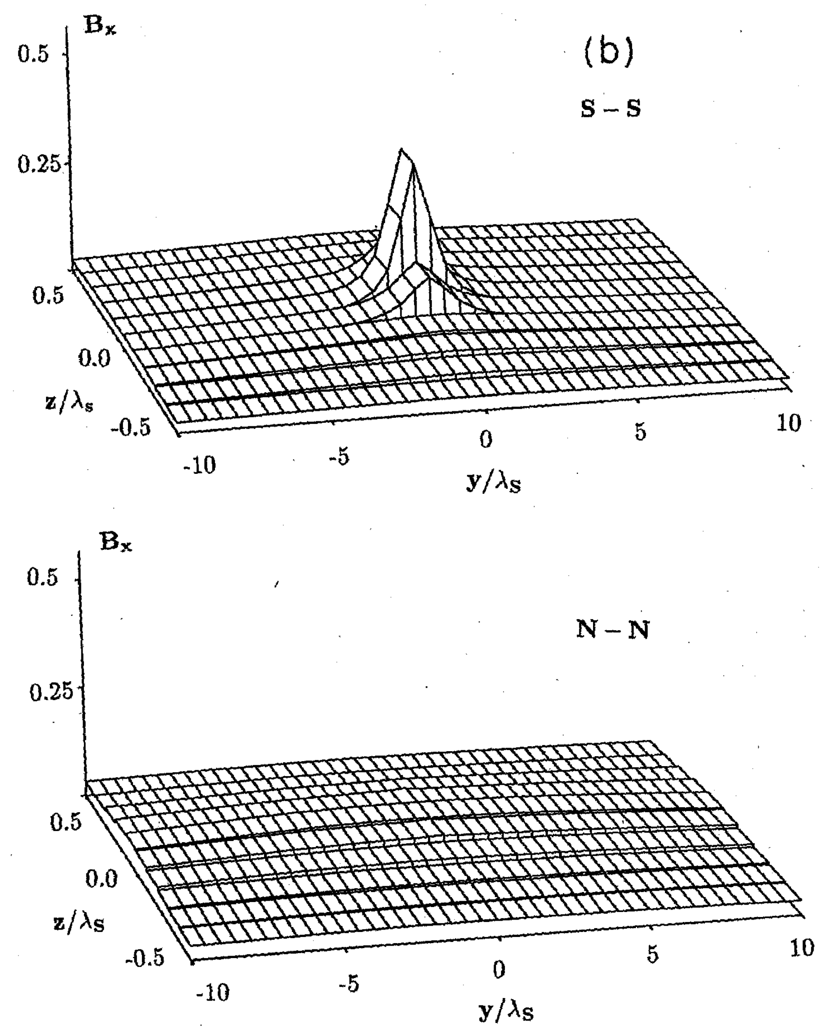

Fig. 8. Magnetic field distribution of a single flux line. The height indicates the magnetic field intensity in arbitrary units. Figures 8(a) and (b) correspond to the cases, $\Gamma_{NN}^2/\lambda_S^2=200$ and 3000, respectively.

In Figs. 8(a) and (b) we show typical results for the field distribution $B_l(y)$ in the case of weak interlayer coupling. As seen in this figure the structure of the single flux line shows clear difference, depending on where the flux line is located in the layer structure. The intensity of the magnetic field near the center of the flux line in the S-S case is larger than that in the N-N case. Consequently the extent of the magnetic field along the layers is larger in the N-N case than in the S-S case, since the total flux should be quantized to the value ϕ_0 in both cases.

Let us next consider the magnetization process near H_{c1}. We assume that the flux lines sit in between adjacent two normal layers along the x-axis and form a regular triangle lattice as shown in Fig. 9. The positions of the flux lines in this case are given by the following two-dimensional vectors on the yz plane,

$$\boldsymbol{r}_{ij}=(\varepsilon_j+ia, jc)\,, \tag{40}$$

where i and j are integers and $\varepsilon_j=0(j=\text{even})$ or $a/2$ ($j=$odd). a and c are the lattice constants of the flux line lattice, respectively, along the y- and z-axes in the rectangu-

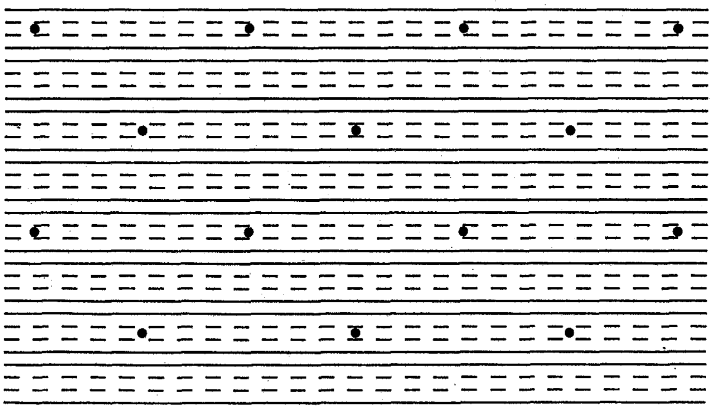

Fig. 9. Structure of the layered superconductor. The layers S and N denote the superconducting and normal layers, respectively.

lar unit cell. In this case the internal field $B_l(y)$ is determined from the equation

$$\partial_y \sin^{-1}\left[\frac{2e}{c}D\Gamma_{l,l+1}^2\partial_y B_l(y)\right]+\frac{2\pi}{cD}[\lambda_{l+1}^2 B_{l+1}(y)-(\lambda_{l+1}^2+\lambda_l^2+D^2)B_l(y)$$
$$+\lambda_l^2 B_{l-1}(y)]=-2\pi\sum_{i,j}\delta_{l,4m_j}\delta(y-\varepsilon_j-ia)\,. \tag{41}$$

From the solution for $B_l(y)$ we can calculate the magnetization by using a thermodynamical relation. In Figs. 10(a), (b) and (c) we plot typical results of the magnetization curves near H_{c1} for different ratios of the inplane penetration depth $\lambda_N{}^2/\lambda_S{}^2$. As seen in this figure, the magnetization curves show remarkable difference from those of conventional type II superconductors. In the case $\lambda_N{}^2/\lambda_S{}^2=2$ (Fig. 10(a)) the gradient $d(-4\pi m)/dh$ is positive at H_{c1}, contrary to that of a conventional type II superconductor without surface pinning. The increase rate of the flux line density for a raised external field is small in this

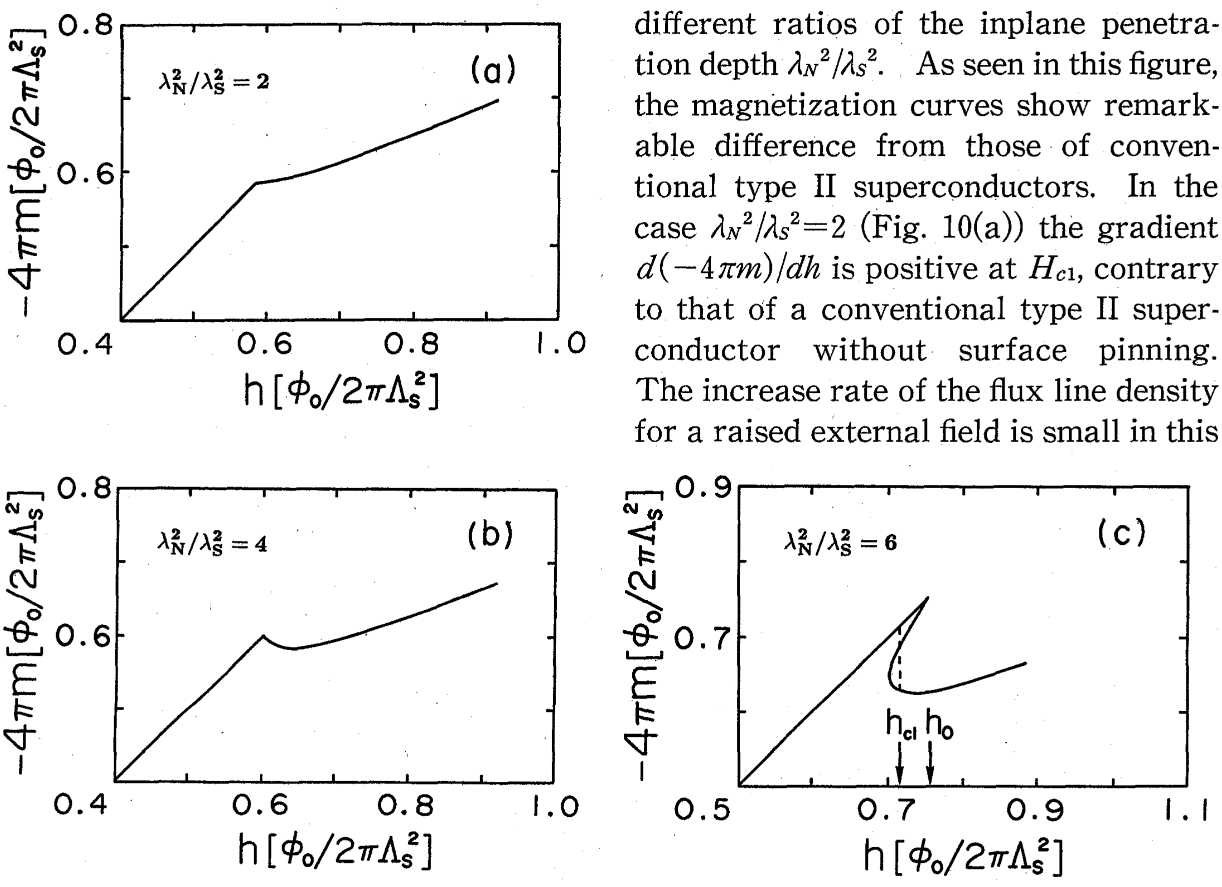

Fig. 10. Magnetization curves in the cases (a) $\lambda_N{}^2=2$, (b) $\lambda_N{}^2=4$ and (c) $\lambda_N{}^2=6$.

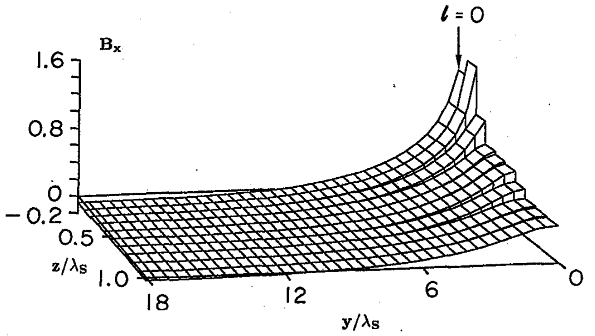

Fig. 11. Spatial distribution of the internal magnetic field in the case where the interaction between flux lines has an attractive part.

case. This result indicates that the strong repulsive interaction works between flux lines. The interaction between flux lines near H_{c1} is caused by the overlap of the internal field created by each flux line. As understood from the field distribution of a single flux line shown in Fig. 8(b), the interaction between flux lines is very anisotropic in layered superconductors. Since the extent of the internal field is larger along the layers, the flux line on the same layer strongly interact with each other. When the value of λ_N/λ_S increases, the gradient $d(-4\pi m)/dh$ rapidly decreases. As seen in Fig. 10(b), the magnetization process near H_{c1} in the case $\lambda_N^2/\lambda_S^2=4$ shows the behavior similar to that of conventional type II superconductors, though the gradient again increases with further increase of the external field. In the case $\lambda_N^2/\lambda_S^2=6$ the magnetization curve changes into a multivalued function of h near H_{c1} (Fig. 10(c)). This result shows that the transition at H_{c1} is first order in this case, that is, the mixed state begins at a finite flux density. This type of magnetization process is found in conventional superconductors with $\kappa\sim1$ (type II/I superconductors), in which the discontinuous transition at H_{c1} originates from the attractive interaction between flux lines. In Fig. 11 the field distribution around a flux line in the flux line lattice is presented at a flux density in the region where the magnetization curve is a multivalued function. It is seen that the field inversion occurs in some region along the layers. This result indicates that the interaction between flux lines on the same layer is attractive. Hence, it is understood that the discontinuous transition at H_{c1} arises from the attractive interaction between flux lines also in layered superconductors. It is noted that the attractive interaction appears in the case where the ratio λ_N/λ_S is large. When the ratio increases, the internal field created by a flux line expands in the direction perpendicular to the layers. Since the total flux created by a flux line is quantized to the value ϕ_0, the expansion of the internal field leads to the decrease of the flux in the region near the center of the flux line. This decrease is caused by the field inversion, as shown in Ref. 6). This field inversion explains the first order transition at H_{c1} seen in the magnetization curve in layered superconductors with inequivalent layers.

References

1) M. Tachiki, S. Takahashi, F. Steglich and H. Adrian, Z. Phys. **B80** (1990), 161.
2) M. Tachiki and S. Takahashi, Physica **B169** (1991), 121.
3) M. Tachiki and S. Takahashi, in *Proceedings of International Conference of Materials and Mechanism High-Temperature Superconductors, Kanazawa, 1991,* to be published in Physica **C**.
4) T. Koyama, N. Takezawa and M. Tachiki, Physica **C172** (1991), 501.
5) T. Koyama, N. Takezawa and M. Tachiki, Physica **C168** (1990), 69.
6) T. Koyama, N. Takezawa and M. Tachiki, Physica **C176** (1991), 567.
7) H. Monien and D. Pines, Phys. Rev. **B41** (1990), 6297.

8) M. Takigawa, P. C. Hammel, R. H. Heffner, Z. Fisk, K. C. Ott and J. D. Thompson, Physica **C162-164** (1989), 853.
9) S. E. Barrett, D. J. Durand, C. H. Pennigton, C. P. Slichter, T. A. Friedmann, J. P. Rice and D. M. Ginsberg, Phys. Rev. **B41** (1990), 6283.
10) T. Koyama and M. Tachiki, Phys. Rev. **B39** (1989), 2297.
11) Y. Kuroda and C. M. Varma, Phys. Rev. **B42** (1990), 8619.
12) P. B. Allen and D. Rainer, Nature **349** (1991), 396.
13) W. W. Warren Jr., R. E. Walstedt, G. F. Brennert, G. P. Espinosa and J. P. Remeika, Phys. Rev. Lett. **59** (1987), 1860.
14) Y. Kitaoka, S. Hiramatsu, T. Kondo and K. Asayama, J. Phys. Soc. Jpn. **57** (1988), 30.
15) T. Imai, T. Shimizu, H. Yasuoka, Y. Ueda and K. Kosuge, J. Phys. Soc. Jpn. **57** (1988), 2280.
16) P. C. Hammel, M. Takigawa, R. H. Heffner, Z. Fisk and K. C. Ott, Phys. Rev. Lett. **63** (1989), 1992.
17) V. V. Moshchalkov, J. Y. Henry, C. Marin, J. Rossat-Mognod and J. F. Jacquot, Physica **C175** (1991), 407.
18) A. F. Khoder, M. Couach, F. Monnier and J. Y. Henry, Europhys. Lett. **15** (1991), 337.